2020 IEEE/RSJ International Conference on Intelligent Robots and Systems (IROS)
October 25-29, 2020, Las Vegas, NV, USA (Virtual)

# Noncontact Estimation of Stiffness Based on Optical Coherence Elastography under Acoustic Radiation Pressure

Yuki Hashimoto[1] and Yasuaki Monnai[1,2]

*Abstract*— **In this study, we propose a method of noncontact elastography, which allows us to investigate stiffness of soft structures by combining optical and acoustic modalities. We use optical coherence tomography (OCT) as a means of detecting internal deformation of a sample appearing in response to a mechanical force applied by acoustic radiation pressure. Unlike most of other stiffness sensing, this method can be performed without any contacts between the sample and actuator that generates pressure. To demonstrate the method, we measure the vibration velocity of a uniform phantom made of polyurethane, and characterize the mechanical parameters. We then confirm that the measured and calculated attenuation of the vibration over the depth agree well, which is inaccessible with a conventional laser Doppler vibrometer. This result paves a way to characterize more complex internal structures of soft materials.**

## I. INTRODUCTION

The evaluation of stiffness of soft structures is important in various fields including biological, medical, and mechanical applications. For example, tissues affected by diseases could be distinguished from normal ones as they often possess different mechanical properties [1]–[3]. It is also known that the spatial distribution of the internal stiffness in human skins plays an important role on tactile perception [4]–[6]. While the detection of internal stiffness has mostly relied on palpation combined with ultrasound imaging or MRI [7]–[10], the recent advancement of the optical coherence tomography (OCT) has opened up a way to observe internal stiffness of samples [11]. Although the observable depth is limited, OCT enables depth mapping of a sample based on optical wave interference with higher resolution than ultrasound and MRI. The internal stiffness can be estimated by detecting deformation caused by an external force. Such a technique is referred to as optical coherence elastography [12]. However, contacting a mechanical probe poses practical limitations in measurement. Since it involves occlusion of the location to be observed with an objective lens, the mechanical force needs to be applied indirectly at a distant point of the sample. The use of a transparent glass as a contact probe has also been attempted, through which the light can be transmitted, but it forces the sample surface to be pressed uniformly despite its original 3D structure [13]. Moreover, targets are sometimes wet, oily, or sticky, and contamination from and to the probe should be prevented.

To circumvent these challenges, we propose fully noncontact optical coherence elastography using acoustic radiation pressure as a means of applying a mechanical force on a sample remotely. The acoustic radiation pressure is based on a nonlinear phenomenon of ultrasound, which acts on an object that intercepts the wave. The pressure is generated by interference of the propagation of ultrasound on the surface of the object. By removing mechanical contact, the OCT observation at the exact point of force application becomes possible without occlusion. Being contamination-free, many different samples can be exchanged quickly under an objective lens.

[1]Yuki Hashimoto and Yasuaki Monnai are with Department of Applied Physics and Physico-Informatics, Keio University, 223-8522 Yokohama, Japan (email: y-hashimoto@keio.jp, monnai@appi.keio.ac.jp). [2]Yasuaki Monnai is also with Japan Science and Technology Agency, PRESTO, 4-1-8 Honcho, Kawaguchi, Saitama, 332-0012, Japan.

## II. METHODS

### A. Phase Sensitive Detection of OCT

In this study, we use a spectral-domain OCT system (TEL220, OCTG-1300, Thorlabs) to detect micro-displacement appearing on top of and inside a sample. The OCT transmits a wide spectrum light toward the inside of a sample, which is backscattered and detected after mixing with a reference signal. The inverse Fourier transform (IFT) of the detected signal generates a reflectivity map in the depth direction of the sample via the calculation of time-of-flight (A-scan). By laterally moving the point of A-scan, we obtain a 2D tomographic image of the sample (B-scan). The system used in this study has the centre wavelength of 1300 nm, maximum sensitivity of 111 dB, axial resolution of 5.5 μm (air), and imaging depth of 3.5 mm (air). Each B-scan consists of 1024 A-scans, and the acquisition time of the single B-scan is 0.56 s.

While the depth map is obtained with the absolute value of the IFT, it has recently been discussed that the difference of the phase parts of the IFT, $\Delta\phi$, between two successive scans contains information of sub-wavelength displacement or vibration. Measurement based on such a phase difference is known as phase sensitive measurement and is equivalent to Doppler measurement [14]–[16]. The velocity map can be calculated by

$$v = \frac{\Delta\phi f_s \lambda}{4n\pi} \tag{1}$$

where $f_s$ is the rate of the A-scans, $\lambda$ is the centre wavelength of the light, $n$ is the refractive index of the sample [17]. In this measurement, 5.5 kHz scan speed and average scan number of 3 (take average of three A-scans) are used; therefore, the effective scan rate is approximately 1.8 kHz. Since polyurethane is used for the sample, we assume that the refractive index of polyurethane is 1.5 [18]. Considering these values, the maximum detectable velocity in this study is calculated as $\frac{f_s\lambda}{4n} = 0.4\,\mathrm{mm\,s^{-1}}$.

978-1-7281-6211-9/20/$31.00 ©2020 IEEE

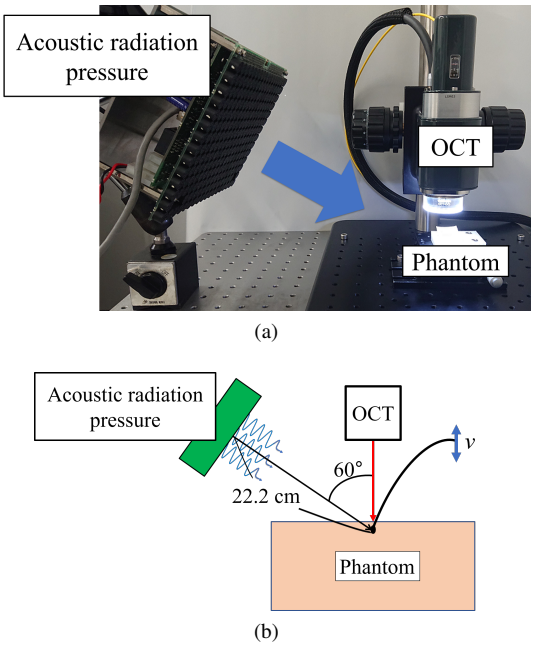


Fig. 1: (a) Experimental setup of noncontact elastography. The acoustic wave radiation pressure is focused onto the surface of the phantom placed under the objective lens of the OCT. (b) Illustration of the mechanical vibration on the phantom surface. The vibration propagates into the depth direction.

### B. Acoustic Radiation Pressure

As a means of noncontanct force application on the sample, we generate acoustic radiation pressure using an ultrasonic phased array transducer [19], [20]. The array consists of 249 pieces of transducers (T4010A, Nippon Ceramic) with the resonant frequency of 40 kHz. By digitally controlling the radiation phase of each transducer in the array, the sound wave can be focused to a single point in free-space. Due to the diffraction limit of the sound of 40 kHz, the focal spot size becomes about 8.5 mm [21]. When the sound pressure of the focus is $p$, the acoustic radiation pressure $P_0$ is given by

$$P_0 = \alpha \frac{p^2}{\rho c^2} \tag{2}$$

where $\rho$ is the density of the medium (air), and $c$ is the sound velocity in the medium, while $\alpha$ is a coefficient that expresses the effect of the reflection by the sample and becomes close to 2 when the impinging ultrasound is mostly reflected. The radiation pressure includes a direct-current component as a result of the nonlinear self-mixing.

In the following experiment, we also apply amplitude modulation to the radiation pressure so that it oscillates with a certain frequency and signal level. When the modulated acoustic radiation pressure impinges on the sample, the sample is mechanically vibrated. By measuring the spatial distribution of the vibration inside the sample appearing in response to a known mechanical pressure using the OCT, we can investigate the stiffness of the sample. It should be noted that the sample placed under the OCT is subject also to small unintentional vibrations caused by the vibration of the table or floor of the laboratory or also by cooling fan of a computer. By setting the modulation frequency of the acoustic radiation pressure different from those unintentional vibration frequencies, we can distinguish the intentional vibration from the unintentional vibration to enhance the signal-to-noise ratio.

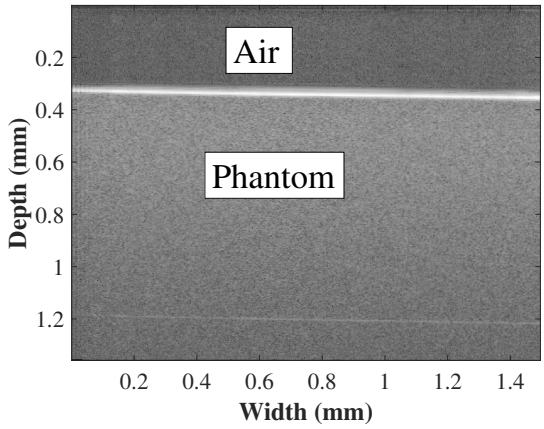


Fig. 2: 2D intensity map on the soft single-layer phantom (phantom A). The phantom is vibrated at 56 Hz, which is the modulation frequency of the acoustic radiation pressure. A-scan is repeated and the results are accumulated along the horizontal axis.

During the experiment, we also noticed that the addition of modulation significantly enhances the brightness of the OCT image. Although detail analysis of this effect is beyond the scope of this paper, this could be explained by the minute surface deformation, which enhances the backscattering of the incident light [22].

### C. Sample Preparation

We use two types of samples made of polyurethane (Exceal, Japan), and the dimensions of the phantoms are approximately 32 mm in length, 22 mm in width, and 5 mm in thickness. The softer sample (phantom A) has the elastic modulus of 0.12 N mm$^{-2}$, and the stiffer one (phantom B) has the elastic modulus of 0.23 N mm$^{-2}$.

Fig. 1 shows the setup to measure the vibration velocity of the phantom under acoustic radiation pressure. The distance and incident angle between the centre of the transducer array and the point of measurement is 22.2 cm and 60°, respectively (Fig. 1 (b)).

## III. RESULTS AND DISCUSSION

### A. Frequency response of vibration velocity in single-layer phantom

We firstly show the intensity map on phantom A obtained by OCT in Fig. 2. The boundary between the air and phantom is visually distinguished by looking at this intensity plot. Next, we extract $\Delta\phi$ between two successive A-scans at a single point vibrated by the acoustic radiation pressure at the frequency of 56 Hz. Fig. 3 shows the extracted phase difference, in which the horizontal axis indicates the elasped time evolution of the phase at the fixed point. Note that no lateral scans are operated in this measurement.

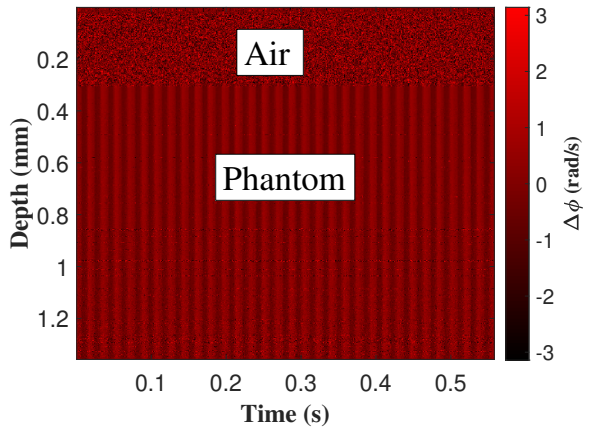


Fig. 3: Temporal sequence of a phase difference depth map at a single point on the soft single-layer phantom (phantom A). The phantom is vibrated at 56 Hz, which is the modulation frequency of the acoustic radiation pressure. A-scan is repeated and the results are accumulated along the horizontal axis.

The phase difference is converted to velocity by (1). We plot the velocity at the surface of the phantom as a function of the elapsed time in Fig. 4 (a). Spatial moving average over a depth interval of 69 µm is taken to reduce the noise effect. We then calculate its Fourier transform to identify the vibration velocity caused by the acoustic radiation pressure at the surface (Fig. 4 (b)). By taking the peak value of Fourier transform at each modulation frequency of acoustic radiation pressure, we plot the velocity amplitude of phantom A with respect to modulation frequency in Fig. 5 (a). The same measurement is performed for the phantom B as shown in Fig. 5 (b).

We model the vibration behaviour based on a distributed mass-spring-damper system (Fig. 6). Assuming sinusoidal oscillation in proportion to $e^{j\omega t}$, where $\omega$ is the angular frequency, the dynamics of the system is described by

$$-\rho\omega^2 u(z) - (E + j\omega\Gamma)\frac{\partial^2 u(z)}{\partial z^2} = 0 \tag{3}$$

where $u(z)$, $\rho$, $E$, and $\Gamma$ denote the displacement, density, Young's modulus, and the viscosity of the phantom, respectively.

The general solution of (3) is described as follows,

$$u(z) = Ae^{-j\omega\sqrt{\frac{\rho}{E+j\omega\Gamma}}z} + Be^{j\omega\sqrt{\frac{\rho}{E+j\omega\Gamma}}z} \tag{4}$$

where the unknown factor $A$ and $B$ are determined by considering two boundary conditions. Firstly, the system is driven at the surface $z = 0$ by a pressure $P_0$ given by (2). Considering the mechanical impedance $Z = \sqrt{E + j\omega\Gamma/\rho}$, which is the ratio of the pressure and velocity in the medium, the velocity at the surface $v(0) = j\omega u(0)$ must be equal to $P_0/Z$, leading to

$$-j\omega\sqrt{\frac{\rho}{E+j\omega\Gamma}}(A - B) = \frac{-P_0}{E+j\omega\Gamma} \tag{5}$$

Secondly, since the phantom is molded in a container, the displacement $u(d)$ at the bottom $z = d$ must be zero, leading to

$$u(d) = Ae^{-j\omega\sqrt{\frac{\rho}{E+j\omega\Gamma}}d} + Be^{j\omega\sqrt{\frac{\rho}{E+j\omega\Gamma}}d} = 0 \tag{6}$$

Combining (5) and (6), we obtain

$$A = \frac{P_0}{j\omega\sqrt{\rho(E+j\omega\Gamma)}}\frac{1}{1+e^{-2j\sqrt{\frac{\rho}{E+j\omega\Gamma}}\omega d}} \tag{7}$$

$$B = \frac{P_0}{j\omega\sqrt{\rho(E+j\omega\Gamma)}}\frac{-e^{-2j\sqrt{\frac{\rho}{E+j\omega\Gamma}}\omega d}}{1+e^{-2j\sqrt{\frac{\rho}{E+j\omega\Gamma}}\omega d}} \tag{8}$$

Hence, the velocity at the surface is given by

$$v(0) = \frac{P_0}{\sqrt{\rho(E+j\omega\Gamma)}}\frac{1-e^{-2j\sqrt{\frac{\rho}{E+j\omega\Gamma}}\omega d}}{1+e^{-2j\sqrt{\frac{\rho}{E+j\omega\Gamma}}\omega d}} \tag{9}$$

Using (9), we plot the fitting curves in Fig. 5. We experimentally obtain the Young's modulus of phantom A and phantom B as: $E_A = 0.12\,\mathrm{N\,mm^{-2}}$, $E_B = 0.25\,\mathrm{N\,mm^{-2}}$. The theoretical values are $0.12\,\mathrm{N\,mm^{-2}}$ and $0.23\,\mathrm{N\,mm^{-2}}$ for phantom A and phantom B. Thus, we see that the noncontact measurement of elasticity is demonstrated.

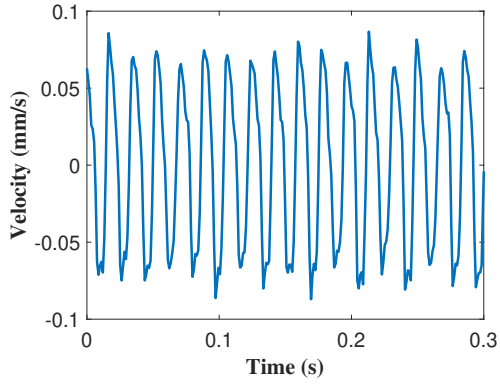


(a)

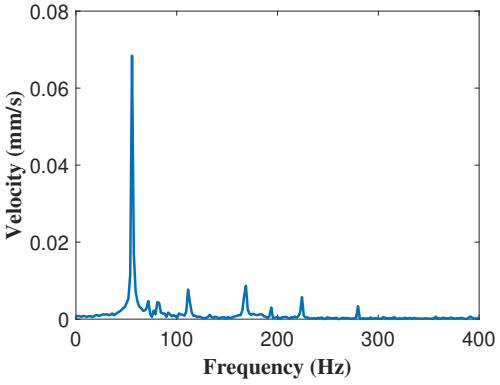


(b)

Fig. 4: (a) Measured velocity at the surface of (spatial average over 69 µm depth is taken) the soft phantom (phantom A) when vibrated by the acoustic radiation pressure of 56 Hz. (b) Amplitude spectrum of the vibration velocity shown in (a) calculated by Fourier transform.

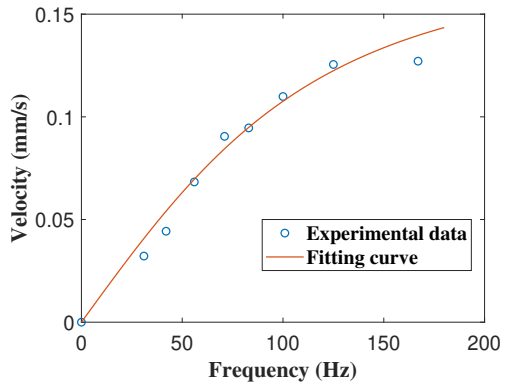


(a)

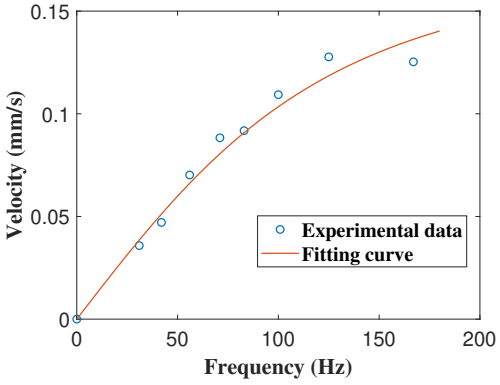


(b)

Fig. 5: Velocity amplitude at the surface of the (a) soft phantom (phantom A) and (b) stiff phantom (phantom B) at a single point with respect to modulation frequency of acoustic radiation pressure. The experimental data are fitted by a theoretical curve derived from (9).

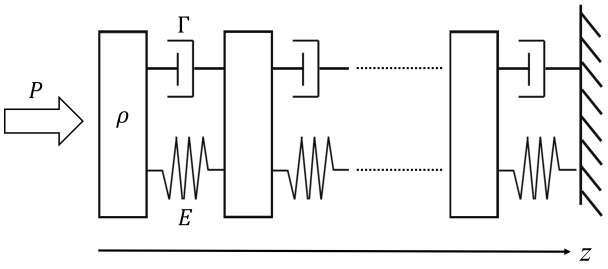


Fig. 6: Mechanical model of a distributed mass-spring-damper model.

## B. Vibration velocity with depth

The measurement same as in Section III-A is performed at each depth to plot the velocity map in the depth direction in Fig. 7, when the modulation frequency is 56 Hz. We choose 56 Hz, because the unintentional vibration is less observed in this frequency. To reduce the noise, we take spatial moving average over the depth range of 69 μm beneath the surface of the phantom.

From (4), the velocity amplitude is theoretically determined as:

$$v(z) = \omega \left( A e^{-j\omega\sqrt{\frac{\rho}{E+j\omega\Gamma}}z} + B e^{j\omega\sqrt{\frac{\rho}{E+j\omega\Gamma}}z} \right) \qquad (10)$$

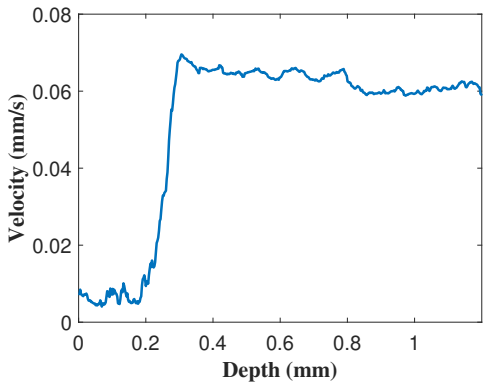


(a)

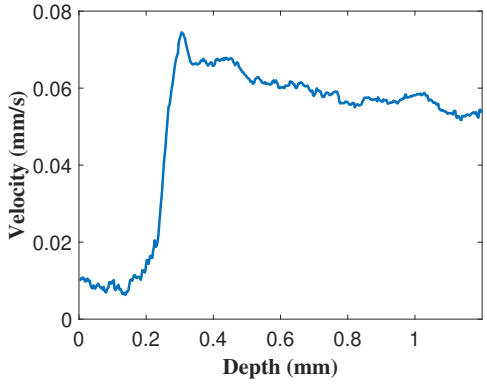


(b)

Fig. 7: Amplitude of velocity with depth in the (a) soft phantom (phantom A) and (b) stiff phantom (phantom B) under 56 Hz modulation frequency of acoustic radiation pressure. The horizontal axis correspond with the depth values in Fig. 3.

Using the parameters identified in Section III-A, we show the theoretical velocity profile in the depth direction in Fig. 8. Although the theoretical and experimental plots are not fully matched in the larger depth, the theoretical decay in the depth direction is reproduced in the experiment. The discrepancy in the larger depth could be explained by the deteriorated signal-to-noise ratio (SNR) for the larger depth in the OCT system.

## C. Vibration velocity with internal rigid material

To explore the potential of the proposed method, We prepare a more complex sample by embedding a piece of a stiff bead in phantom B. The bead is made of polystyrene and has a diameter of 2.9 mm. Fig. 9 shows the intensity map. The bead is placed 0.2 mm beneath the surface of the phantom. We vibrate this phantom using the acoustic radiation pressure with the frequency of 56 Hz. We obtain the velocity maps in the depth direction at multiple lateral positions, and integrate them to visualize as Fig. 10. Thus, we can quantitatively observe that the velocity in the bead is smaller than in the phantom while the distance from the phantom surface to the bead is smaller than the bead diameter. Although further analysis will be investigated in our future work, this measurement enables to extract mechanical information of

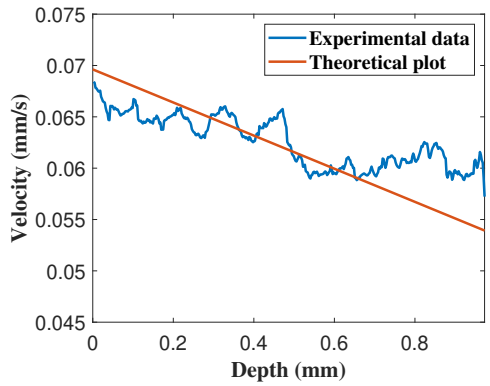


(a)

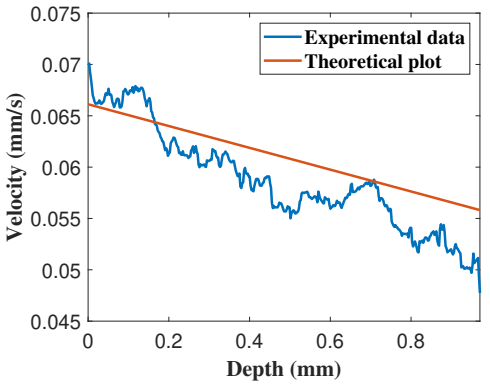


(b)

Fig. 8: Amplitude of velocity with depth beneath the surface of the (a) soft phantom (phantom A) and (b) stiff phantom (phantom B) under 56 Hz modulation frequency of acoustic radiation pressure. Note that 0 mm depth indicates the surface of the phantoms.

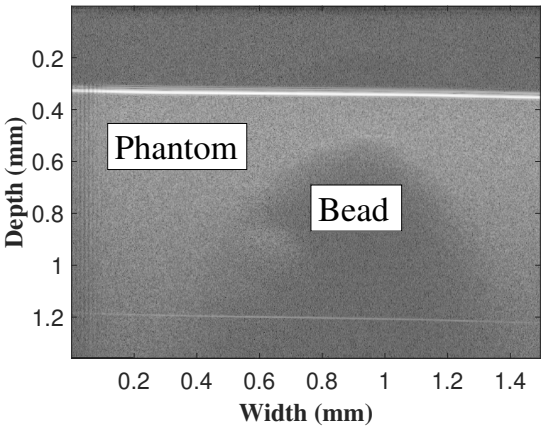


Fig. 9: 2D Intensity map in phantom B with a bead. A-scan is repeated and the results are accumulated along the horizontal axis.

multi-layered stiffness distribution inside the phantom.

## IV. CONCLUSIONS

We have demonstrated noncontact method to estimate the stiffness of phantom, namely applying acoustic radiation pressure on the surface and measuring vibration velocity by OCT. Young's moduli of two types of phantoms are estimated from the frequency response of vibration velocity using a mass-spring-damper model. We also have observed the velocity behaviour with depth, which can be done by investigating inside the phantom. Subsequently, a rigid substance inside the phantom is used to illustrate the effectiveness of this internal vibration measurement.

In this study, we use homogeneously distributed single-layer phantoms. However, the mechanical characteristics of the measured sample is expected to extend more sophisticated and heterogeneous phantoms in future work, by implementing the OCT with a different feature such as shorter source wavelength and rigorously evaluating the boundary condition. Our noncontact technique promises great potential to fulfill the needs of internal measurements in many fields including biological and clinical applications.

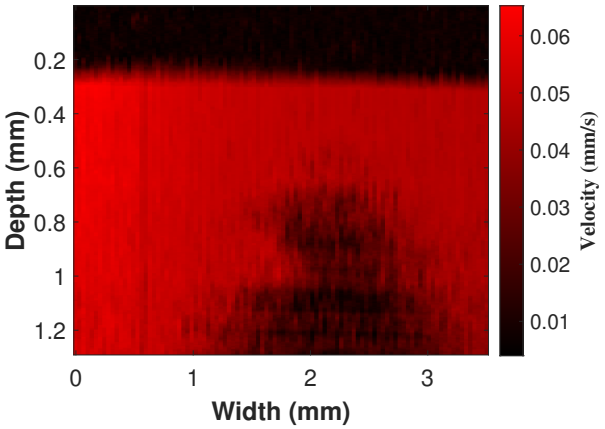


Fig. 10: 2D velocity map in phantom B with a bead under 56 Hz modulation frequency of acoustic radiation pressure. Velocity amplitude is measured at 100 lateral positions in the range of 3.5 mm width. Spatial moving average over the depth range of 69 µm is taken. Colour bar indicates the velocity amplitude.

## ACKNOWLEDGMENT

This work was supported by Japan Science and Technology Agency, PRESTO Grant Number JPMJPR18J9, Japan.

## REFERENCES

[1] W. Xu, R. Mezencev, B. Kim, L. Wang, J. McDonald, and T. Sulchek, "Cell stiffness is a biomarker of the metastatic potential of ovarian cancer cells," *PloS one*, vol. 7, no. 10, 2012.

[2] G. Wang, W. Mao, R. Byler, K. Patel, C. Henegar, A. Alexeev, and T. Sulchek, "Stiffness dependent separation of cells in a microfluidic device," *PloS one*, vol. 8, no. 10, pp. 1–10, 2013.

[3] H.-H. Lin, H.-K. Lin, I.-H. Lin, Y.-W. Chiou, H.-W. Chen, C.-Y. Liu, H. I.-C. Harn, W.-T. Chiu, Y.-K. Wang, M.-R. Shen, *et al.*, "Mechanical phenotype of cancer cells: Cell softening and loss of stiffness sensing," *Oncotarget*, vol. 6, no. 25, p. 20 946, 2015.

[4] J. Z. Wu, R. G. Dong, S. Rakheja, A. Schopper, and W. Smutz, "A structural fingertip model for simulating of the biomechanics of tactile sensation," *Medical engineering & physics*, vol. 26, no. 2, pp. 165–175, 2004.

[5] R. S. Dahiya, G. Metta, M. Valle, and G. Sandini, "Tactile sensing—from humans to humanoids," *IEEE transactions on robotics*, vol. 26, no. 1, pp. 1–20, 2009.

[6] S. M. Pasumarty, S. A. Johnson, S. A. Watson, and M. J. Adams, "Friction of the human finger pad: Influence of moisture, occlusion and velocity," *Tribology Letters*, vol. 44, no. 2, p. 117, 2011.

[7] K. R. Nightingale, M. L. Palmeri, R. W. Nightingale, and G. E. Trahey, "On the feasibility of remote palpation using acoustic radiation force," *The Journal of the Acoustical Society of America*, vol. 110, no. 1, pp. 625–634, 2001.

[8] K. Nightingale, M. S. Soo, R. Nightingale, and G. Trahey, "Acoustic radiation force impulse imaging: In vivo demonstration of clinical feasibility," *Ultrasound in medicine & biology*, vol. 28, no. 2, pp. 227–235, 2002.

[9] A. J. Romano, J. A. Bucaro, R. Ehnan, and J. J. Shirron, "Evaluation of a material parameter extraction algorithm using mri-based displacement measurements," *IEEE transactions on ultrasonics, ferroelectrics, and frequency control*, vol. 47, no. 6, pp. 1575–1581, 2000.

[10] J. F. Greenleaf, M. Fatemi, and M. Insana, "Selected Methods for Imaging Elastic Properties of Biological Tissues," *Annual Review of Biomedical Engineering*, vol. 5, no. 1, pp. 57–78, 2003.

[11] B. F. Kennedy, P. Wijesinghe, and D. D. Sampson, "The emergence of optical elastography in biomedicine," *Nature Photonics*, vol. 11, no. 4, p. 215, 2017.

[12] B. F. Kennedy, R. A. McLaughlin, K. M. Kennedy, L. Chin, A. Curatolo, A. Tien, B. Latham, C. M. Saunders, and D. D. Sampson, "Optical coherence microelastography: mechanical-contrast imaging of tissue microstructure," *Biomedical Optics Express*, vol. 5, no. 7, p. 2113, 2014.

[13] K. M. Kennedy, S. Es'haghian, L. Chin, R. A. McLaughlin, D. D. Sampson, and B. F. Kennedy, "Optical palpation: Optical coherence tomography-based tactile imaging using a compliant sensor," *Optics letters*, vol. 39, no. 10, pp. 3014–3017, 2014.

[14] R. K. Wang, Z. Ma, and S. J. Kirkpatrick, "Tissue doppler optical coherence elastography for real time strain rate and strain mapping of soft tissue," *Applied Physics Letters*, vol. 89, no. 14, p. 144 103, 2006.

[15] B. R. White, M. C. Pierce, N. Nassif, B. Cense, B. H. Park, G. J. Tearney, B. E. Bouma, T. C. Chen, and J. F. De Boer, "In vivo dynamic human retinal blood flow imaging using ultra-high-speed spectral domain optical doppler tomography," *Optics express*, vol. 11, no. 25, pp. 3490–3497, 2003.

[16] R. K. Wang, S. Kirkpatrick, and M. Hinds, "Phase-sensitive optical coherence elastography for mapping tissue microstrains in real time," *Applied Physics Letters*, vol. 90, no. 16, p. 164 105, 2007.

[17] R. A. Leitgeb, R. M. Werkmeister, C. Blatter, and L. Schmetterer, "Doppler Optical Coherence Tomography," *Progress in Retinal and Eye Research*, vol. 41, pp. 26–43, 2014.

[18] A. S. Abed, K. M. Ziadan, and A. Q. Abdullah, "Some optical properties of polyurethane," *Iraqi J. of Polymers*, vol. 17, no. 1, pp. 18–28, 2014.

[19] T. Hoshi, M. Takahashi, T. Iwamoto, and H. Shinoda, "Noncontact tactile display based on radiation pressure of airborne ultrasound," *IEEE Transactions on Haptics*, vol. 3, no. 3, 2010.

[20] K. Hasegawa and H. Shinoda, "Aerial display of vibrotactile sensation with high spatial-temporal resolution using large-aperture airborne ultrasound phased array," in *2013 World Haptics Conference, WHC 2013*, 2013.

[21] K. Hasegawa, L. Qiu, A. Noda, S. Inoue, and H. Shinoda, "Electronically steerable ultrasound-driven long narrow air stream," *Applied Physics Letters*, vol. 111, no. 6, 2017.

[22] S. Wang and K. V. Larin, "Noncontact depth-resolved micro-scale optical coherence elastography of the cornea," *Biomedical Optics Express*, vol. 5, no. 11, p. 3807, 2014.